Thermal and chemical evolution of the subarc mantle revealed by spinel-hosted melt inclusions in boninite from the Ogasawara (bonin) Archipelago, Japan

メタデータ	言語: eng
	出版者:
	公開日: 2017-10-03
	キーワード (Ja):
	キーワード (En):
	作成者:
	メールアドレス:
	所属:
URL	https://doi.org/10.24517/00010764

Publisher: GSA
Journal: GEOL: Geology
DOI:10.1130/G36191.1

Thermal and chemical evolution of the subarc mantle revealed by spinel-hosted melt inclusions in boninite from the Ogasawara (Bonin) Archipelago

Susumu Umino[1], Keitaro Kitamura[1], Kyoko Kanayama[1], Akihiro Tamura[1], Naoya Sakamoto[2], Osamu Ishizuka[3], and Shoji Arai[1]

[1]Division of Natural System, Kanazawa University, Kanazawa, Ishikawa 920-1192, Japan

[2]Creative Research Institution, Hokkaido University, Sapporo, Hokkaido 001-0021, Japan

[3]Geological Survey of Japan, Advanced Industrial Science and Technology, Tsukuba, Ibaraki 305-8567, Japan

ABSTRACT

Primitive melt inclusions in chrome spinel from the Ogasawara Archipelago comprise two discrete groups of high-SiO_2, MgO (high-Si) and low-SiO_2, MgO (low-Si) boninitic suites with ultra-depleted dish- and V-shaped, and less depleted flat rare earth element (REE) patterns. The most magnesian melt inclusions of each geochemical type were used to estimate the T-P conditions for primary boninites, that range from 1345°C-0.56 GPa to 1421°C-0.85 GPa for the 48-46 Ma high-Si and low-Si boninites, and 1381°C-0.85 GPa for the 45 Ma low-Si boninite. The onset of the Pacific Slab subduction at 52 Ma forced upwelling of depleted mid-ocean ridge basalt mantle (DMM) to yield proto-arc basalt (PAB). With the rise of DMM, refractory harzburgite ascended without melting. At 48-46 Ma, introduction of slab fluids induced melting of the PAB residue and high-T harzburgite, resulted in the low-Si and high-Si boninites, respectively. Meanwhile, convection within the mantle wedge brought the less depleted residue

of PAB and DMM into the region fluxed by slab fluids, which melted to yield the less depleted low-Si boninite at 45 Ma, and fertile arc basalts, respectively.

INTRODUCTION

The Izu-Ogasawara (Bonin)-Mariana (or IBM) Arc has been a locus of intense study on oceanic arc evolution because it provides complete records of the volcanic arc development since the onset of the Pacific Plate subduction beneath the Philippine Sea Plate up to present (e.g., Ishizuka et al., 2006, 2011). Along the entire IBM forearc MORB-like proto-arc basalt (PAB; Reagan et al., 2010) extruded at 52-48 Ma, followed by arc tholeiitic lavas on the Ogasawara Archipelago (Umino et al., 2009). The dissected tholeiitic rocks are overlain by 48-46 Ma highly depleted, high-silica boninite with minor low-silica boninite (Maruberiwan Formation), which became covered with less depleted, low-silica boninite associated with calc-alkalic magmas at 45 Ma (Mikazukiyama Formation). By 44 Ma the volcanic front retreaded westward and fertile arc magmas (Hahajima Island Group basalt, or HGB) superseded boninites (Kanayama et al., 2012; 2014). This variation in magma geochemistry represents the thermo-chemical evolution of the mantle wedge during the establishment of the IBM arc.

Boninites potentially provide significant constraints on the P-T-X conditions of the varying mantle wedge because of their primitive compositions compatible with refractory upper mantle minerals (Umino, 1986; Crawford et al., 1989; Pearce et al., 1992; Kanayama et al., 2012). Specifically, melt inclusions in forsteritic olivine in boninite have been used for estimating primary magma compositions, based on which Tongan low-Si boninite was proposed to derive from hot mantle plumes with a mantle potential T (MPT) >1500°C (e.g., Sobolev & Danyushevsky, 1994; Sobolev and Chaussidon, 1996). However, most olivine-hosted melt inclusions suffered post-entrapment crystallization and diffusive reequilibration with the hosts, which are irreversible by heating experiments (Kamenetsky et al., 2002; Kent, 2008). Especially Fe-loss is critical in estimating T-P conditions of primary boninite. Therefore, the original melt compositions upon entrapment were restored by raising FeO to the liquid line of descent, which was assumed to be equal to bulk compositions. Unfortunately, bulk compositions of porphyritic arc magmas like boninites mostly differ from the liquid compositions due to processes such as crystal accumulation and imperfect fractionation, and mixing of magmas.

In contrast, chrome spinel is an excellent container of primitive magmas because the trapped liquid compositions are little modified by crystallization of the host spinel due to limited Cr contents in melts (e.g., Shimizu et al., 2001). Furthermore, chrome spinel is resistant to deterioration compared to silicate minerals such as olivine, and chemically stable against low-grade metamorphic alteration. Chrome spinel is also eminently pressure-resistant as it may preserve ultra-high-pressure minerals (Yamamoto et al., 2009), so it is expected that chrome spinel may preserve primitive compositions of inclusions trapped under high temperatures and pressures.

This paper focuses on primitive melts preserved in chrome spinel, the earliest crystallized phase from boninite magmas in the Ogasawara Archipelago (Umino, 1986), to estimate the genetic conditions for primary magmas, and discusses the thermo-chemical evolution of the mantle wedge during the early stages of the IBM subduction zone development.

SPINEL-HOSTED MELT INCLUSIONS

Mode of Occurrence of Melt Inclusions

Boninites are widely exposed on the Mukojima and Chichijima islands, Ogasawara Archipelago, where chrome spinel samples were taken from the beach sand “Uguisu-zuna”, natural mineral concentrates of orthopyroxene and minor amounts of olivine, spinel +/-

clinopyroxene (Umino et al., 2009). Poorly developed river systems and generally consistent geochemistry and mineralogy of Uguisu-zuna and the surrounding geology support the view that those mineral concentrates were eroded from the nearby exposures and wave-sorted (Fig. DR-1). Melt inclusions are randomly distributed within spinel and have mainly oval or rounded triangular shapes constrained by crystallographic orientation of the host spinel. This indicates a primary origin for these inclusions trapped during the growth of the host spinel (Schiano, 2003). All melt inclusions in a single spinel crystal have the same texture and geochemical characteristics, indicating that these inclusions were trapped at the same time and experienced the same cooling history during ascent and quenching upon eruption.

Melt inclusions consist of glass with or without crystals. 21% of the inclusions examined are of entirely homogeneous glass (Figs. 1A, B, DR-2A, B) with or without shrinkage bubbles on the wall. The rest 79% carry daughter or captured crystals in addition to glass. Rare melt inclusions develop an outer zone of rapidly grown daughter pyroxene crystals surrounding a homogeneous glass pool in the core (Figs. 1C, DR-2C). However, both the outer zone and the core have identical bulk major element compositions (Fig. DR-3). About 27% of inclusions are “variolitic”, composed entirely of variolitic pyroxene crystals, interstitial glass and vesicles (Figs. 1D, DR-2D). Both the “melt (glass)” dominant inclusions and the variolitic inclusions lack any compositional gradient through the inclusions and in the adjacent host spinel (Figs. 1, DR-2). The textural relationships and chemical homogeneity of these melt inclusions strongly suggest that the primary melt compositions at the time of entrapment are well preserved, in spite of the postentrapment crystallization in some inclusions. We therefore take the bulk compositions of these melt-dominant and variolitic inclusions as representative of quenched pristine melt compositions.

Major and Trace Element Geochemistry

The melt inclusions have 52-63 wt% SiO_2, 7-23 wt% MgO and 0.01-0.25 wt% TiO_2 on an anhydrous basis (Fig. 2; Table DR-1). With few exceptions, almost all fit the category of boninite defined by the IUGS (SiO_2 >52 wt%, MgO >8 wt% and TiO_2 <0.5 wt%; Le Maitre, 2002). Most inclusions form two roughly subparallel groups showing an inverse correlation of MgO and SiO_2, which are generally consistent with fractionation paths of olivine followed by orthopyroxene (based on alphaMELTS by Smith and Asimow, 2005), combined with mixing of melts on the paths (Figs. 2A, DR-5). One group with higher MgO and SiO_2 falls within the field of high-silica boninite of Kanayama et al. (2012), but are more Mg-rich than the whole rocks at a given SiO_2 ("high-Si (boninitic) inclusions", hereafter). The other group is somewhat scattered but plot between the high-Si inclusions and the bulk low-Si boninites, and are hence called "low-silica (low-Si) (boninitic) inclusions". Almost all high-Si inclusions have low CaO (<8 wt%) and CaO/Al_2O_3 ratios <0.8, characteristics of low-Ca boninite (Crawford, 1989). On the other hand, the low-Si inclusions have 6.5-12 wt% CaO and spread over the fields of both low-Ca and high-Ca boninites.

High-Si boninitic inclusions are severely depleted in REEs with chondrite-normalized patterns, which can be divided into dish-shaped (high-Si-D) and V-shaped (high-Si-V) at a Gd/Yb ratio of 0.7 (Fig. 2B). Dish-shaped REE patterns are identical to those of the bulk boninites in overall shape and abundance (Fig. DR-6). On the contrary, V-shaped REE patterns have never been found among the bulk rocks. High-Si-D and high-Si-V inclusions are enclosed in spinel with Cr/ (Cr + Al) of 0.85-0.91 and TiO_2 <0.12 wt% derived from the Maruberiwan

Formation. Although individual spinel grains have only a single type of inclusions, both high-Si-D and high-Si-V inclusions coexist in spinel samples from the same locality.

The low-Si boninitic inclusions are of two distinct types. One has less depleted, flat REE patterns with low Zr/Ti <0.02 (low-Si-F), and is only found in spinel derived from the Mikazukiyama Formation (Fig. 2C). Most of them possess a high-Ca boninitic affinity with CaO/Al_2O_3 ratios >0.8. The other type, low-Si-D inclusions, is found in spinel from the Maruberiwan Formation and shows depleted dish-shaped REE patterns with variable Zr/Ti ratios (0.01-0.03), CaO (6-11 wt%) and CaO/Al_2O_3 ratios (0.5-1). The host spinel of the low-Si inclusions has low Cr/ (Cr + Al) of 0.72-0.87 and 0.04-0.24 wt% TiO_2.

The variolitic melt inclusions (Fig. 1D) tend to show lower H_2O contents (<2.4 wt%) and H_2O/Ce ratios than the other inclusions (Fig. DR-4), suggesting water loss due to degassing. We therefore corrected water contents of variolitic samples by assuming their original H_2O/Ce ratios to be equal to the average H_2O/Ce ratios of undegassed samples of the same geochemical type. Because all low-Si-F inclusions exhibit a variolitic texture, the H_2O contents were restored based on the maximum H_2O/Ce ratio of the type, which gives the minimum H_2O estimates. The restored H_2O and H_2O/Ce ratios mostly range from 2 to 5 wt% and 9800-43200, respectively.

Genetic Conditions of Primary Boninites

If magma retains its primary composition, it should be multiply saturated with olivine and orthopyroxene at the temperature and pressure of segregation, which can be estimated by the combination of appropriate geothermobarometers. We applied the method of Putirka (2008) based on olivine-liquid equilibration (Putirka et al., 2007) and olivine-orthopyroxene-liquid equilibration (Putirka, 2008). Olivine-spinel equilibria suggests oxygen fugacity of boninite magma to be 0 to +1 in log unit above fayalite-magnetite-quartz (FMQ) buffer (Evans et al., 2012), whereas Fe^{3+}/Fe^{2+} ratios of pillow margin glass estimated by XANES (Ishibashi et al., 2012) and sulfur speciation of melt inclusions in spinel determined by soft X-ray photoelectron spectroscopy (Shimizu et al., 2014) indicate f_{O2} of $\Delta\log(FMQ) = +1 \sim +2$ for the Ogasawara boninite. We therefore assumed f_{O2} of $\Delta\log(FMQ) = 1\pm1$ for the T-P estimates. CO_2 concentrations of boninitic melt inclusions in chrome spinel from the Ogasawara Archipelago are very low (<50 ppm; Shimizu and Shimizu, 2013) and hence H_2O is considered as the only volatile species. The compositions of primary boninite magmas are assumed to be those of the most magnesian melt inclusions among the four geochemical types described above, i.e. high-Si-D, high-Si-V, low-Si-D and low-Si-F melt inclusions (Table DR-1). The estimated equilibration T and P are 1343-47°C at 0.54-0.59 GPa for the low-Si-D boninite, and 1415-28°C at 0.74-0.96 GPa for the high-Si-D and high-Si-V boninites (Fig. 3). The genetic T-P of 1378-1384°C and 0.81-0.88 GPa for the low-Si-F boninite are considered to be the maximum estimates, because its H_2O content is the minimum estimate.

DISCUSSION

There is a general consensus that boninitic magmas derive from severely depleted source mantle which experiences flux melting by introduction of hydrous fluids (or melts) liberated from a descending slab (e.g. Pearce et al. 1992; Bédard, 1999; Kanayama et al., 2012). These studies ascribed high Zr/Ti ratios of high-Si boninites to contribution of slab melt under amphibolite facies. The degree of depletion of the source mantle can be assessed by concentrations of heavy REEs such as Yb, which are predominantly immobile through slab dehydration and sediment partial melting. Figure 4 shows Yb-Zr/Ti variations modeled by 5% and 20% batch partial melts of residual DMM (Workman and Hart, 2005) after extraction of 0% to 20% fractional melts, mixed with 5% batch partial melt of amphibolitic slab (based on altered oceanic basalt at Site 1149; Kelley et al., 2003). The model indicates that Yb concentrations are more sensitive to the degree of source depletion than that of batch melting. Both the PAB and the HGB have the least depleted source mantle and little contribution from slab melts. Irrespective to the degree of melting of the residual DMM, the highest Yb and the least Zr/Ti for the 45 Ma low-Si-F inclusions indicate less than 11-16% source depletion and contribution of 8-15% slab melt, smallest among all melt inclusions. The 48-46 Ma high-Si-D and high-Si-V inclusions have the least Yb and the highest Zr/Ti, indicating the largest source depletion up to 19-24% and mixing of 10-20% slab melt. Although the 48-46 Ma low-Si-D inclusions are similarly low in Yb, the model suggests slightly lower depletion of 17-20%.

Subsidence of the old, dense Pacific Plate caused forearc spreading and decompression melting of DMM-like asthenosphere to form MORB-like PAB magma for the first few million years after the subduction initiated (Ishizuka et al., 2011; Kanayama et al., 2012). If the PAB source had a MPT of ~1410°C, which is slightly above the present suboceanic ambient mantle (Herzberg et al., 2007), the residue would become ~1345°C at 0.5 GPa, coincident with the T-P conditions for the 48-46 Ma low-Si-D boninite magma, supporting the remelting of the PAB residue (Fig. 3). However, it is incompatible with the coexistence of extremely hot (>1400°C at 0.8 GPa), severely depleted source mantle of the high-Si boninite magmas. If, as the plume-origin model of boninite suggests, the pre-boninite decompression melting of the DMM was solely responsible for the extreme depletion of the boninite source, it should have ascended from the depth of 3.5 GPa with a MPT of 1500°C. The ascent of such high-T peridotite to <1 GPa should cause extensive decompression melting to produce picritic magmas, which have never been found among the pre-boninite PAB. This indicates that the depleted proto-boninite source already existed below the DMM-like PAB source before the subduction began. This is supported by the unradiogenic Os isotopic composition of harzburgite drilled in the Izu Forearc, which experienced melt extraction in Proterozoic age and became the source for the IBM boninite magmas (Parkinson et al., 1998; Suzuki et al., 2011). With the DMM asthenosphere, the refractory harzburgitic source ascended along the adiabatic decompression path without melting, resulted in the high temperatures of the high-Si boninites (Fig. 3). Considering 1380°C and 0.8 GPa are the maximum estimates for the low-Si-F boninite genesis, it would be close to the adiabatic melting path of the PAB source. Compared to the low-Si-D boninite, the low-Si-F boninite has the higher T-P and less depleted source, suggesting its derivation from the periphery of the asthenospheric upwelling, which suffered lower degrees of melting and ascended off the forearc spreading axis. By 45 Ma, convection in the wedge mantle driven by drag force of the subducting slab brought the less depleted low-Si-F boninite source and DMM-like asthenosphere into the region fluxed by slab fluids, which melted to generate the low-Si-F boninite magma, and then arc tholeiitic and calc-alkalic magmas on the Hahajima Island Group and the western scarps of the Ogasawara Ridge.

ACKNOWLEDGMENTS

This study was supported by the Geological Survey of Japan and MEXT Special Budget Project No. 812000009 to S.A. and No. 25287133 to O.I. We thank N. Yurimoto (Hokkaido University) for the usage of SIMS, and N. Chatterjee, A.J. Arculus and F. Sorbadere for their critical reviews.

REFERENCES CITED

Bédard, J.H., 1999, Petrogenesis of boninites from the Betts Cove Ophiolite, Newfoundland, Canada: Identification of subducted source components: Journal of Petrology, v. 40, p. 1853–1889, doi:10.1093/petroj/40.12.1853.

Crawford, A.J., Falloon, T.J., and Green, D.H., 1989, Classification, petrogenesis and tectonic setting of boninites, *in* Crawford, A.J., ed., Boninites and Related Rocks: London, Unwyn-Hyman Ltd., p. 1–49.

Evans, K.A., Elburg, M.A., and Kamenetsky, V.S., 2012, Oxydation state of subarc mantle: Geology, v. 40, 783 - 786.

Grove, T.L., Chatterjee, N., Parman, S.W., and Médard, E., 2006, The influence of H_2O on mantle wedge melting: Earth and Planetary Science Letters, v. 249, p. 74–89, doi:10.1016/j.epsl.2006.06.043.

Grove, T.L., Till, C.B., Lev, E., Chatterjee, N., and Méard, E., 2009, Kinematic variables and water transport control the formation and location of arc volcanoes: Nature, v. 459, p. 694–697, doi:10.1038/nature08044.

Herzberg, C., Asimow, P.D., Arndt, N., Niu Y., Lesher, C.M., Fitton, J.G., Cheadle, M.J., and Saunders, A.D., 2007. Temperatures in ambient mantle and plumes: Constraints from basalts, picrite, and komatiites: Geochemistry, Geophysics, Geosystems, v. 8, Q02006, doi: 10.1029/2006GC001390.

Herzberg, C., and Gazel, E., 2009, Petrological evidence for secular cooling in mantle plumes: Nature, v. 458, p. 619–622, doi:10.1038/nature07857.

Ishibashi, H., Odake, S., Kanayama, K., Hamada, M., and Kagi, H., 2013. The redox states of basaltic and boninitic magmas erupted at the early stage of the Bonin arc formation; Fe-K edge XANES study: IAVCEI Scientific Meeting 2013, Kagoshima.

Ishizuka, O., Kimura, J., Li, Y.B., Stern, R.J., Reagan, M.K., Taylor, R.N., Ohara, Y., Bloomer, S.H., Ishii, T., Hargrove III, U.S., and Haraguchi, S., 2006, Early stages in the evolution of Izu-Bonin arc volcanism: New age, chemical, and isotopic constraints: Earth and Planetary Science Letters, v. 250, p. 385–401, doi:10.1016/j.epsl.2006.08.007.

Ishizuka, O., Tani, K., Reagan, M.K., Kanayama, K., Umino, S., Harigane, Y., Sakamoto, I., Miyajima, Y., Yuasa, M., and Dunkley, D.J., 2011, The timescales of subduction initiation and subsequent evolution of an oceanic island arc: Earth and Planetary Science Letters, v. 306, p. 229–240, doi:10.1016/j.epsl.2011.04.006.

Kamenetsky, V.S., Sobolev, A.V., Eggins, S.M., Crawford, A.J., and Arculus, R.J., 2002, Olivine-enriched melt inclusions in chromites from low-Ca boninites, Cape Vogel, Papua New Guinea: evidence for ultramafic primary magma, refractory mantle source and enriched components: Chemical Geology, v. 183, p. 287–303.

Kanayama, K., Umino, S., and Ishizuka, O., 2012, Eocene volcanism during the incipient stage of Izu–Ogasawara Arc: Geology and petrology of the Mukojima Island Group, the Ogasawara Islands: The Island Arc, v. 21, p. 288–316, doi:10.1111/iar.12000.

Kanayama, K., Umino, S., and Ishizuka, O., 2014, Shallow submarine volcano group in the early stage of island arc development: Geology and petrology of small islands south off Hahajima main island, the Ogasawara Islands: Journal of Asian Earth Sciences, v. 85, p. 1–25, doi:10.1016/j.jseaes.2014.01.012.

Kelley, K.A., Plank, T., Ludden, J., and Staudigel, H., 2003, Composition of altered oceanic crust at ODP sites 801 and 1149: Geochemistry Geophysics Geosystems, v. 4, doi:10.1029/2002GC000435.

Kent, A.J.R., 2008, Melt inclusions in basaltic and related volcanic rocks, *in* Putirka, K.D., and Teply, F.J. III, eds., Reviews in Mineralogy and Geochemistry 69, p. 273–331.

Le Maitre, R.W., ed., 2002, Igneous Rocks, A Classification And Glossary Of Terms: Recommendations Of The International Union Of Geological Sciences Subcommission On The Systematics Of Igneous Rocks: Cambridge, Cambridge University Press, p. 236.

Parkinson, I.J., Hawkesworth, C.J., and Cohen, A.S., 1998, Ancient mantle in a modern arc: Osmium isotopes in Izu-Bonin-Mariana forearc peridotites: Science, v. 281, p. 2011–2013, doi:10.1126/science.281.5385.2011.

Pearce, J.A., van der Laan, S.R., Arculus, R.J., Murton, B.J., Ishii, T., Peate, D.W., and Parkinson, I.J., 1992, Boninite and harzburgite from Leg 125 (Bonin-Mariana forearc): a case study of magma genesis during the initial stages of subduction, *in* Fryer, P., Pearce, J.A., Stokking, L.B., et al., eds., Proceedings of Ocean Drilling Program, Scientific Results, volume 125: College Station, TX, Ocean Drilling Program, p. 623–659.

Putirka, K., 2008, Thermometers and Barometers for Volcanic Systems, *in* Putirka, K.D., and Teply, F.J. III, eds., Reviews in Mineralogy and Geochemistry, v. 69, p. 61–120.

Putirka, K.D., Perfit, M., Ryerson, F.J., and Jackson, M.G., 2007, Ambient and excess mantle temperatures, olivine thermometry, and active vs. passive upwelling: Chemical Geology, v. 241, p. 177–206, doi:10.1016/j.chemgeo.2007.01.014.

Reagan, M.K., Ishizuka, O., Stern, R.J., Kelley, K.A., Ohara, Y., Blichert-Toft, J., Bloomer, S.H., Cash, J., Fryer, P., Hanan, B.B., Hickey-Vargas, R., Ishii, T., Kimura, J., Peate, D.W., Rowe, M.C., and Woods, M., 2010, Fore-arc basalts and subduction initiation in the Izu-Bonin-Mariana system: Geochemistry Geophysics Geosystems, v. 11, p. Q03X12, doi:10.1029/2009GC002871.

Schiano, P., 2003, Primitive mantle magmas recorded as silicate melt inclusions in igneous minerals: Earth-Science Reviews, v. 63, p. 121–144, doi:10.1016/S0012-8252(03)00034-5.

Shimizu, K., and Shimizu, N., 2013, Volatile behavior in an immature subduction zone inferred from boninitic melt inclusions in Cr-spinel: Goldschmidt 2013, Florence, Abstracts, 07c.

Shimizu, K., Komiya, T., Hirose, K., Shimizu, N., and Maruyama, S., 2001, Cr-spinel, an excellent micro-container for retaining primitive melts — implications for a hydrous plume origin for komatiites: Earth and Planetary Science Letters, v. 189, p. 177–188, doi:10.1016/S0012-821X(01)00359-4.

Shimizu, K., Kashiwabara, T., and Tamenori, Y., 2014, Oxidation state of magmas at an immature subduction zone-inferred from sulfur speciation of boninitic and tholeiitic melt inclusions: Sacramento, Goldschmidt 2014, Abstracts, 08d.

Smith, P.M., and Asimow, P.D., 2005, Adiabat_1ph: A new public front-end to the MELTS, pMELTS, and pHMELTS models: Geochemistry Geophysics Geosystems, v. 6, p. Q02004, doi:10.1029/2004GC000816.

Sobolev, A.V., and Chaussidon, M., 1996, H_2O concentrations in primary melts from supra-subduction zones and mid-ocean ridges: Implications for H_2O storage and recycling in the mantle: Earth and Planetary Science Letters, v. 137, p. 45–55, doi:10.1016/0012-821X(95)00203-O.

Sobolev, A.V., and Danyushevsky, L.V., 1994, Petrology and Geochemistry of Boninites from the North Termination of the Tonga Trench: Constraints on the Generation Conditions of Primary High-Ca Boninite Magmas: Journal of Petrology, v. 35, p. 1183–1211, doi:10.1093/petrology/35.5.1183.

Suzuki, K., Senda, R., and Shimizu, K., 2011, Osmium behavior in a subduction system elucidated from chromian spinel in Bonin Island beach sands: Geology, v. 39, p. 999–1002, doi:10.1130/G32044.1.

Taylor, R.N., Nesbitt, R.W., Vidal, P., Harmon, R.S., Auvray, B., and Croudace, I.W., 1994, Mineralogy, chemistry, and genesis of the Boninite series volcanics, Chichijima, Bonin Islands, Japan: Journal of Petrology, v. 35, p. 577 - 618.

Umino, S., 1986, Magma mixing in boninite sequence of Chichijima, Bonin Islands: Journal of Volcanology and Geothermal Research, v. 29, p. 125–157, doi:10.1016/0377-0273(86)90042-9.

Umino, S., Nakano, S., Ishizuka, O., and Komazawa, M., 2009, Geological Map of Japan 1:200,000, Ogasawara Shotô (in Japanese with English abstract): Geological Survey of Japan, AIST.

Workman, R.K., and Hart, S.T., 2005, Major and trace element composition of the depleted MORB mantle (DMM): Earth and Planetary Science Letters, v. 231, p. 53–72, doi:10.1016/j.epsl.2004.12.005.

Yamamoto, S., Komiya, T., Hirose, K., and Maruyama, S., 2009, Coesite and clinopyroxene exsolution lamellae in chromites: In-situ ultrahigh-pressure evidence from podiform chromitites in the Luobusa ophiolite, southern Tibet: Lithos, v. 109, p. 314–322, doi:10.1016/j.lithos.2008.05.003.

FIGURE CAPTIONS

Figure 1. Representative COMPO images (left) and electron microprobe analyzer (EMPA) elemental maps showing textures, and Fe and Mg distributions respectively of melt inclusions

and the host chrome spinel. Note the absence of Fe-rich and Mg-poor halos in the spinel host adjacent to the melt inclusions, confirming the absence of diffusive Fe-loss from the melt.

Figure 2. Boninitic melt inclusions (circles and squares) compared with bulk boninites (crosses) of the 48-46 Ma Maruberiwan (Mb) and 45 Ma Mikazukiyama (Mk) Formations from Ogasawara. Examples of fractionation paths for primary boninites (solid and broken lines) are shown at 0.2 GPa and fO_2 of 0.5 log unit above fayalite-magnetite-quartz (FMQ) buffer using alphaMELTS (A), chondrite-normalized REE patterns of high-Si-D and high-Si-V (B) and low-Si-D and low-Si-F (C) inclusions. Broken lines encircle the bulk boninites. See Fig. DR-5 for further explanation.

Figure 3. T-P estimates of multiple saturation for the primary boninite magmas. The ranges of T-P estimates denote 1σ of H_2O and f_{O2} of $\Delta\log(FMQ) = 1\pm1$. Note that varying f_{O2} by 2 in log unit brings a little difference in T-P estimates, but increase in H_2O content by 1 wt% reduces the estimated T and P by 34°C and 0.17 GPa, respectively. Adiabatic melting paths are after Herzberg and Gazel (2009). The broken arrow is that for the DMM asthenosphere with MPT = 1410°C. The solid arrow is an adiabatic decompression path of the harzburgite source for the high-Si boninite, calculated using dT/dP = 13.3 °C/GPa (Putirka et al., 2007). The harzburgite solidus is based on the residual DMM after 20% fractional melting by alphaMELTS.

Figure 4. Yb vs Zr/Ti of boninitic melt inclusions compared with pre-boninite PAB, bulk boninites and post-boninite HGB. Symbols are the same as in Fig. 2. The Yb-Zr/Ti relationships is modeled by mixing of 5% (gray) and 20% (black) batch partial melts of residual DMM after extraction of 0-20% fractional melts (denoted such as “10%”), and 5% batch partial melt of amphibolitic slab (based on altered oceanic basalt at Site 1149; Kelley et al., 2003) with a proportion of clinopyroxene: amphibole:plagioclase = 7:88:5 (Taylor et al., 1994). Numbers on

the broken lines (“70:30”, etc.) are the proportions of peridotite melt:slab melt. Increase in slab melting up to 15% does not change the model results.

[1] GSA Data Repository item 2014xxx, Boninitic melt inclusions in chrome spinel from the Ogasawara Archipelago, is available online at www.geosociety.org/pubs/ft2014.htm, or on request from editing@geosociety.org or Documents Secretary, GSA, P.O. Box 9140, Boulder, CO 80301, USA.

Fig. 1

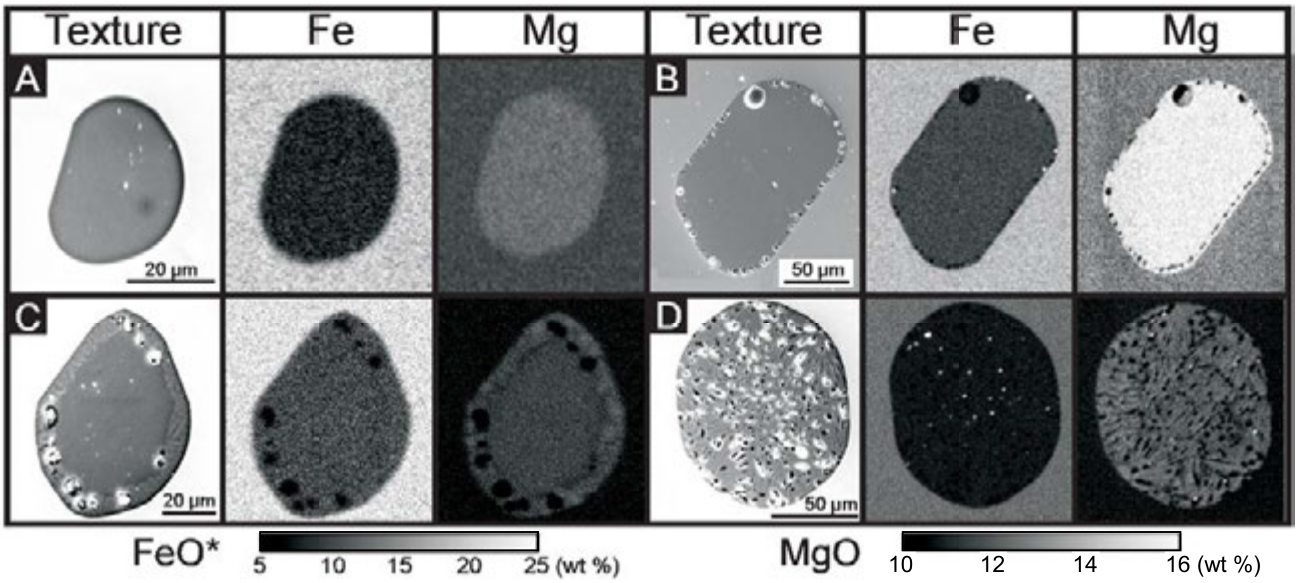
Texture
Fe
Mg
Texture
Fe
Mg
A
20 μm
B
50 μm
C
20 μm
D
50 μm
FeO*
5
10
15
20
25 (wt %)
MgO
10
12
14
16 (wt %)

Fig. 2

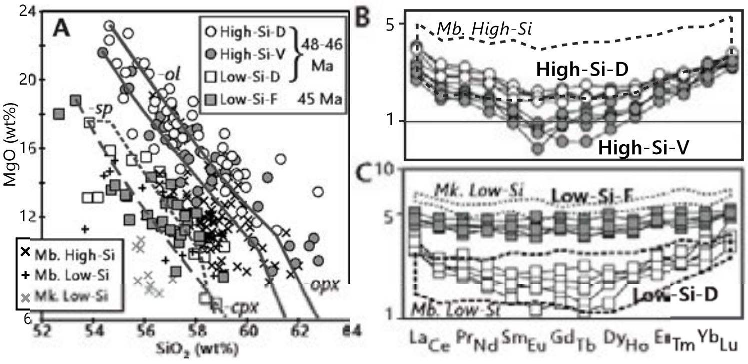
A
B
C
MgO (wt%)
SiO$_2$ (wt%)
24
20
16
12
6
52
54
56
58
60
62
64
High-Si-D
High-Si-V
Low-Si-D
Low-Si-F
48-46 Ma
45 Ma
Mb. High-Si
Mb. Low-Si
Mk. Low-Si
-ol
-sp
-cpx
opx
5
1
10
Mb. High-Si
High-Si-D
High-Si-V
Mk. Low-Si
Low-Si-F
Low-Si-D
Mb. Low-Si
La
Ce
Pr
Nd
Sm
Eu
Gd
Tb
Dy
Ho
Er
Tm
Yb
Lu

Fig. 3

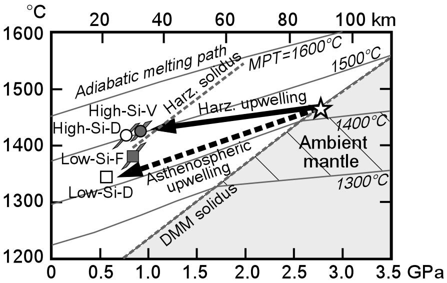
°C
20
40
60
80
100 km
1600
1500
1400
1300
1200
0
0.5
1.0
1.5
2.0
2.5
3.0
3.5 GPa
Adiabatic melting path
Harz. solidus
MPT=1600°C
1500°C
1400°C
1300°C
High-Si-V
High-Si-D
Low-Si-F
Low-Si-D
Harz. upwelling
Asthenospheric upwelling
Ambient mantle
DMM solidus

Fig. 4

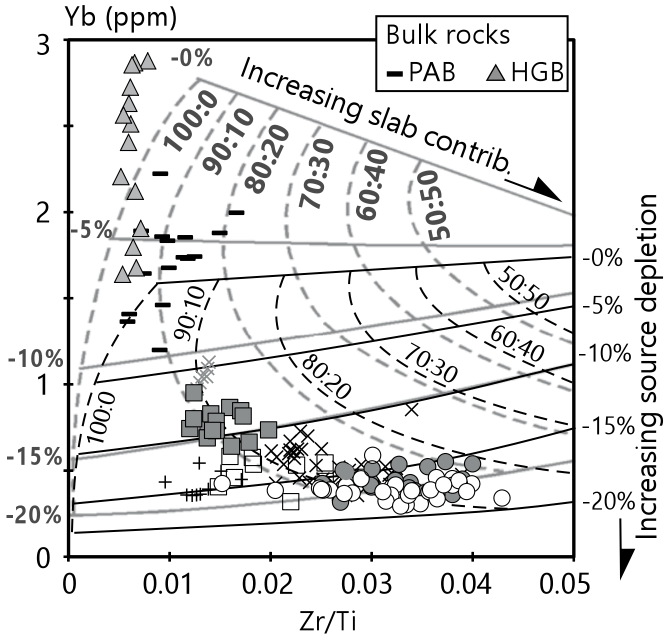
Yb (ppm)
Bulk rocks
▬ PAB
▲ HGB
-0%
Increasing slab contrib.
100:0
90:10
80:20
70:30
60:40
50:50
-5%
-10%
-15%
-20%
-0%
-5%
-10%
-15%
-20%
Increasing source depletion
100:0
90:10
80:20
70:30
60:40
50:50
3
2
1
0
0
0.01
0.02
0.03
0.04
0.05
Zr/Ti

Data Repository

BONINITIC MELT INCLUSIONS IN CHROME SPINEL FROM THE OGASAWARA ARCHIPELAGO

DATA REPOSITORY for "Thermal and chemical evolution of the subarc mantle revealed by spinel-hosted melt inclusions in boninite from the Ogasawara (Bonin) Archipelago" by Susumu Umino, Keitaro Kitamura, Kyoko Kanayama, Akihiro Tamura, Naoya Sakamoto, Osamu Ishizuka, and Shoji Arai.

Analytical methods and procedures

Chrome spinels were handpicked under binocular after cleaning and sieving the sand samples with pure water. Spinel crystals embedded in epoxy resin on a slide glass were ground and polished to expose the core of crystals with melt inclusions, which were utilized for major and trace element analyses, including H_2O (Table DR-1).

Major elements of glass and minerals were analyzed by a JEOL JXA-8800 electron probe microanalyzer (EPMA) at Kanazawa University. The accelerating voltage was 15 kV and the specimen current was 12 nA. Analyses of glass followed the procedures of Noguchi *et al.* (2004) using broad beam diameters <30 μm. The corrections were made according to ZAF method. Relative errors (1σ) of melt inclusion analyses are better than 0.4% for SiO_2, 11.3% for TiO_2, 1.3% for Al_2O_3, 3.0% for FeO, 23.3% for MnO, 1.2% for MgO, 1.7% for CaO, 7.8% for Na_2O, 7.9% for K_2O and 6.7% for Cr_2O_3.

Trace element compositions (REEs, V, Cr, Co, Ni, Li, B, Sc, Rb, Sr, Y, Zr, Nb, Cs, Ba, Hf, Ta, Pb, Th and U) of glass were analyzed by laser ablation (193 nm ArF excimer: MicroLas GeoLas Q-plus) inductively coupled plasma mass spectrometry (Agilent 7500s) (LA-ICP-MS) at Kanazawa University (Morishita et al., 2005a, b). Each analysis was performed by ablating spots of 30 or 40 μm in diameter at 5 Hz with energy density of 8 J/cm^2 per pulse. Signal integration times were 50 seconds for a gas background interval and 50 seconds for an ablation interval. BCR-2G (USGS glass reference material) was used as the primary calibration standard and its element concentration values are selected from the GeoReM database (see Jochum and Nohl., 2008). Repeated analyses of NIST 610, NIST612 and BIR show that reproducibility is better than ±11% (1 σ) except B, Cs, Ta and U (Table DR-2). Data reduction was facilitated using ^{29}Si as internal standards for glass, based on SiO_2 contents obtained by EPMA analysis, and followed a protocol essentially identical to that outlined by Longerich et al. (1996). Details of the analytical method and data quality for the LA-ICP-MS system at Kanazawa University are described in Morishita et al. (2005a, b) and Ichiyama et al. (2013).

H_2O concentrations in glass of melt inclusions were determined by using a Secondary Ion Mass Spectrometry (SIMS) Cameca IMS-6F of the Creative Research Institution, Hokkaido University. Analytical procedures followed Miyagi and Yurimoto (1995) using natural hornblende with 1.66 wt% H_2O as a standard. Water contents (in wt%) were determined by comparing $^{1}H/^{30}Si$ ratios of unknown samples with averages of those of the standard hornblende measured on the same day.

Water content

H_2O contents vary from 1 to 5 wt% and H_2O/Ce ratios from 2000 to 43200. Interstitial glass in melt inclusions consisting mainly of variolitic pyroxene crystals and vesicles (Fig. 1D) tends to show lower H_2O concentrations (<2.4 wt%). These glass inclusions have consistently lower H_2O/Ce ratios compared to glass in melt inclusions comprising pure glass and a few shrinkage vesicles of the same geochemical type (Fig. DR-4). H_2O and Ce do not fractionate during partial melting of the source mantle and fractional crystallization of magmas due to their similar partition coefficients between melt and relevant mineral phases (Michael, 1995; Hauri et al., 2006), and hence melt inclusions of the same geochemical type are expected to have similar H_2O/Ce ratios. Thus, the coincidence of the variolitic texture and the lower H_2O contents and H_2O/Ce ratios compared to those of pure glass inclusions of the same geochemical type suggests that the variolitic melt inclusions experienced degassing and partially lost their original water during ascent to the surface. We therefore have corrected water contents of degassed samples and estimated the original water contents based on Ce contents, by assuming the original H_2O/Ce ratios of the degassed samples to be equal to the average H_2O/Ce ratio of undegassed samples of the same geochemical type. Because all low-Si-F (flat chondrite-normalized REE pattern) inclusions show a variolitic texture with low H_2O/Ce ratios, the original H_2O/Ce ratio of the type was assumed to be 9800, the maximum ratio among Type F inclusions observed. This gives the minimum estimates of the original H_2O contents for low-Si-F inclusions. The restored H_2O contents range from 1 to 6 wt% with restored H_2O/Ce ratios varying from 9800 to 43200.

Procedure of T-P estimate of olivine-orthopyroxene multiple saturation

T-P estimates for the primary boninitic magmas to be multiply saturated with olivine and orthopyroxene were determined by solving simultaneously the olivine-liquid geothermobarometry (equation (4) of Putirka et al., 2007) and olivine-orthopyroxene-liquid geothermobarometry (equation (42) of Putirka, 2008), following the procedure described in Putirka (2008). Major element compositions including Fe_2O_3, and H_2O contents are used as input. First, (1) The Fe^{3+}/Fe^{2+} ratio at prescribed f_{O2} (here $\Delta\log(FMQ) = 0$ to +2) and the liquidus temperature is determined by using alphaMELTS (Smith and Asimow, 2005) at initial guess of pressure. (2) T and P obtained from the geothermobarometry are then used to calculate Fe^{3+}/Fe^{2+} ratio at prescribed f_{O2} by alphaMELTS. (1) and (2) are repeated iteratively until T, P, and Fe^{3+}/Fe^{2+} ratio become stable within 0.5%. Varying f_{O2} by 2 in log unit brings a little difference in T-P estimates compared to the uncertainty inherited from the geothermobarometry, while increase in H_2O content by 1 wt% reduces the estimated T and P by 34°C and 0.17 GPa, respectively.

REFERENCES

Falloon, T.J., and Danyushevsky, L.V., 2000, Melting of refractory mantle at 1.5, 2 and 2.5 GPa under anhydrous and H2O-saturated conditions: Implications for the petrogenesis of high-Ca boninites and the influence of subduction components on mantle melting: Journal of Petrology, v. 41, p. 257–283.

Hauri, E.H., Gaetani, G.A., and Green, T.H., 2006, Partitioning of water during melting of the Earth's upper mantle at H_2O-undersaturated conditions: Earth and Planetary Science Letters, v. 248, 715–734.

Ichiyama, Y., Morishita, T., Tamura, A., and Arai, S., 2013, Petrology of peridotite xenolith-bearing basaltic to andesitic lavas from the Shiribeshi Seamount, off northwestern Hokkaido, the Sea of Japan: Journal of Asian Earth Sciences, v. 76, p. 48–58.

Jochum, K. P., and Nohl, U., 2008, Reference materials in geochemistry and environmental research and the GeoReM database: Chemical Geology, v. 253, p. 50–53.

Longerich, H.P., Jackson, S.E. and Gunther, D., 1996, Laser ablation inductively coupled plasma mass spectrometric transient signal data acquisition and analyte concentration calculation: Journal of Analytical Atomic Spectrometry, v. 11, p. 899–904.

Michael, P., 1995, Regionally distinctive sources of depleted MORB: Evidence from trace elements and H_2O: Earth and Planetary Science Letters, v. 131, p. 301–320.

Miyagi, I., and Yurimoto, H., 1995, Water content of melt inclusions in phenocrysts using Secondary Ion Mass Spectrometer: Bulletin of Volcanological Society of Japan, v. 40, p. 349–355.

Morishita, T., Ishida, Y., and Arai, S., 2005a, Simultaneous determination of multiple trace element compositions in thin (<30 μm) layers of BCR-2G by 193 nm ArF excimer laser ablation-ICP-MS: implications for matrix effect and elemental fractionation on quantitative analysis: Geochemical Journal, v. 39, p. 327–40.

Morishita, T., Ishida, Y., Arai, S., and Shirasaka, M., 2005b, Determination of multiple trace element compositions in thin (30 μm) layers of NIST SRM 614 and 616 using laser ablation-inductively coupled plasma-mass spectrometry (LA-ICP-MS): Geostandrand and Geoanalytical Research, v. 29, p. 107-122.

Noguchi, S., Morishita, T., and Toramaru, A., 2004, Corrections for Na-loss on micro-analysis of glasses by electron probe X-ray micro analyzer (in Japanese with English abstract): Japanese Magazine of Mineralogical and Petrological Sciences, v. 33, p. 85–95.

Smith, P.M., and Asimow, P.D., 2005, Adiabat_1ph: A new public front-end to the MELTS, pMELTS, and pHMELTS models: Geochemistry, Geophysics, Geosystems, v. 6, Q02004, doi:10.1029/2004GC000816.

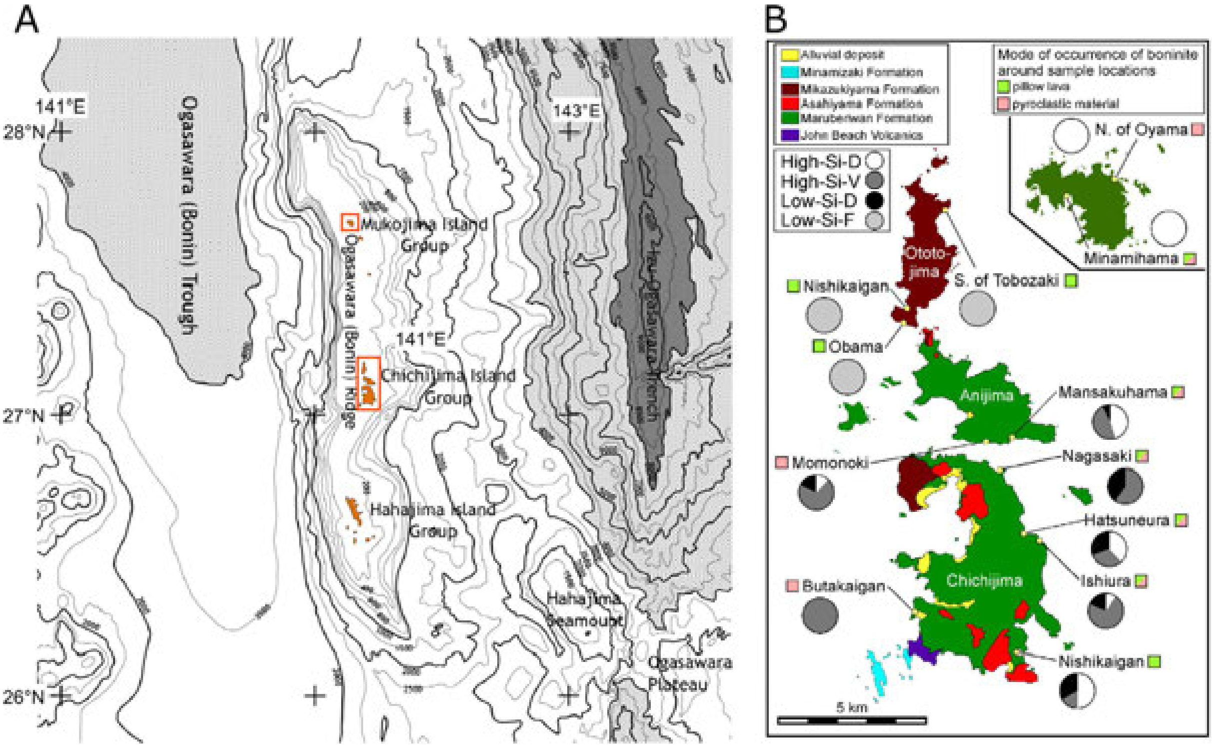

Figure DR-1. Locations of the Ogasawara Archipelago (A) and samples of chrome spinel together with the mode of occurrence of the host rocks and geochemical types (B).

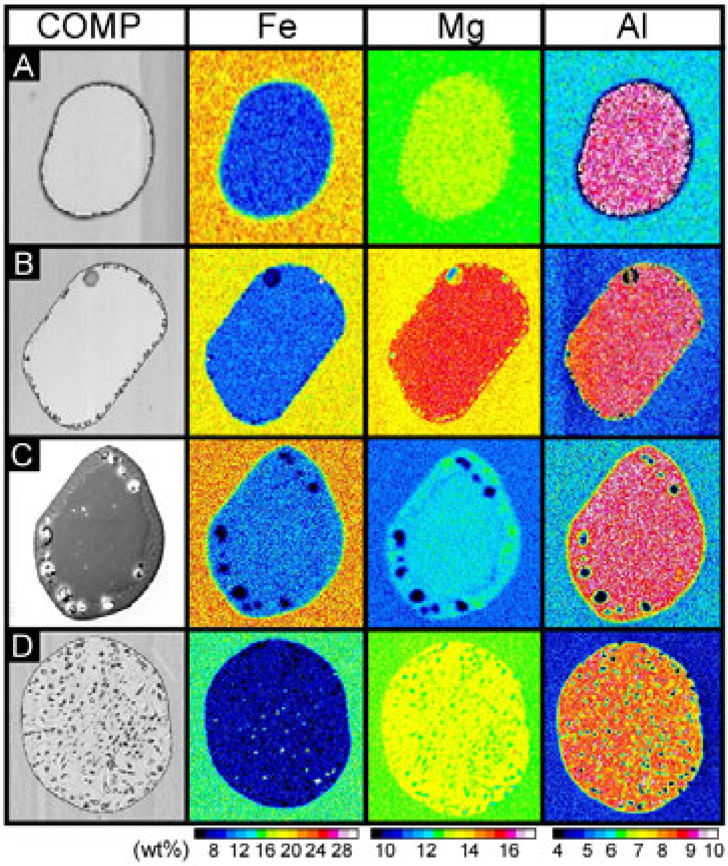

Figure DR-2. SEM (COMPO) images (left) and pseudo-colored EMPA maps (right) of Fe, Mg, and Al of melt inclusions and the host chrome spinel shown in Figure 1. Note the absence of Fe-rich and Mg-poor halos in the spinel host adjacent to the melt inclusions, confirming the absence of diffusive Fe-loss from the melt.

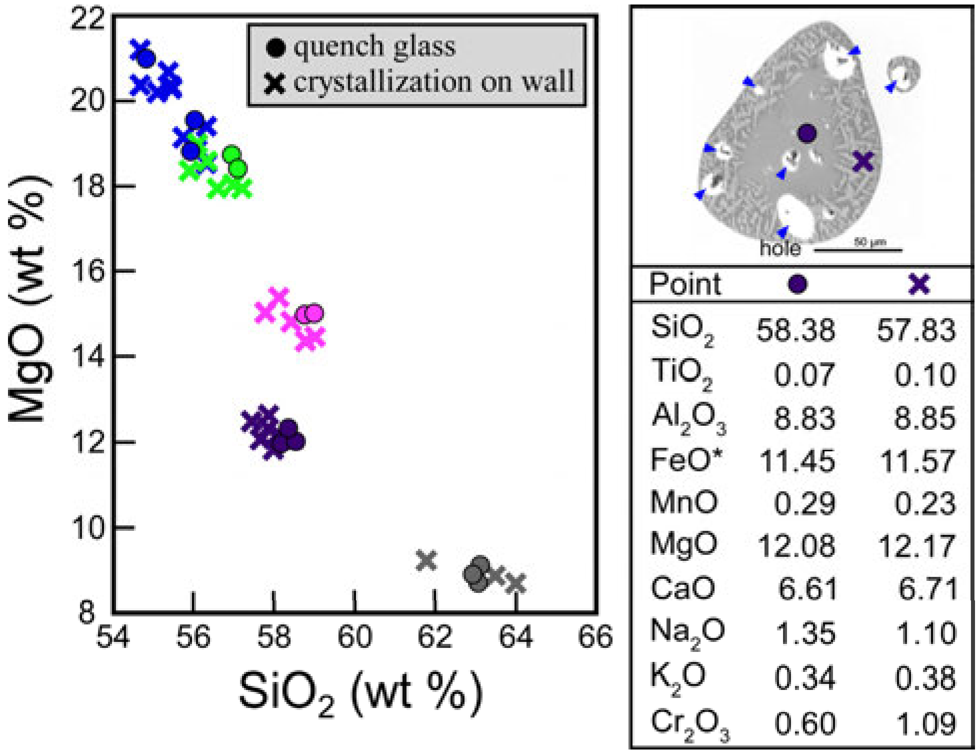

Point	●	×
SiO_2	58.38	57.83
TiO_2	0.07	0.10
Al_2O_3	8.83	8.85
FeO*	11.45	11.57
MnO	0.29	0.23
MgO	12.08	12.17
CaO	6.61	6.71
Na_2O	1.35	1.10
K_2O	0.34	0.38
Cr_2O_3	0.60	1.09

Figure DR-3. Analyses of melt inclusions (left) composed of the central glass pool (dots) surrounded by an outer zone with quench crystals and interstitial glass (crosses). A SEM image (upper right) shows dark grey glass rimmed by a zone with light grey quench crystals. Bright spots are holes (blue arrows) due to edge effect. Symbols with the same colors are analyses of the same inclusions. Note that both outer zones and central glass pools have identical bulk compositions, indicating that crystallization of the outer zone did not affect the composition of the remaining melt in the core.

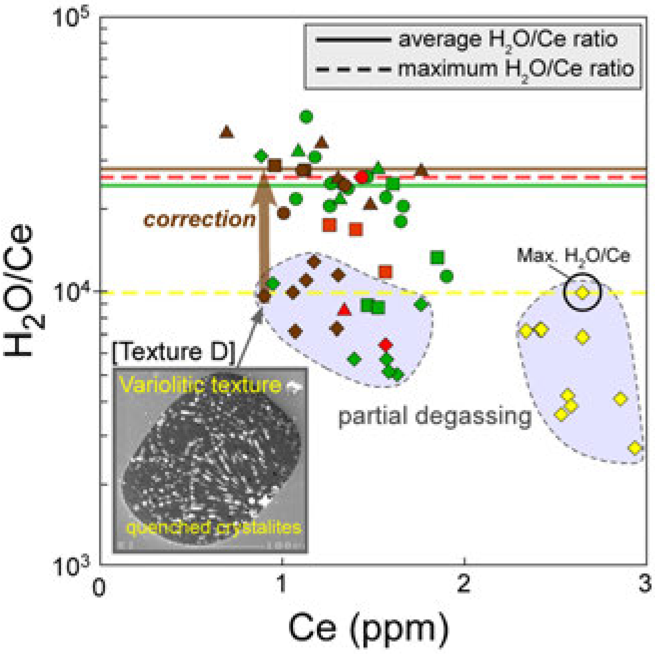

Figure DR-4. H_2O/Ce plotted against Ce of melt inclusions of high-Si-D (green) and high-Si-V (brown), and low-Si-D (red) and low-Si-F (yellow). Variolitic inclusions (solid diamonds) (Figs. 1D, DR-2D) have consistently lower H_2O/Ce ratios compared to glass in melt inclusions comprising pure glass and a few shrinkage vesicles (circles, squares and triangles) (Figs. 1A, 1B, 1C, DR-2A, 2B, 2C) of the same geochemical type. These variolitic inclusions are considered to have partly lost their water upon entrapment due to degassing. For these inclusions, the original water contents were restored based on Ce contents, by assuming the original H_2O/Ce ratios of the variolitic samples to be equal to the average H_2O/Ce ratio of undegassed samples of the same geochemical type.

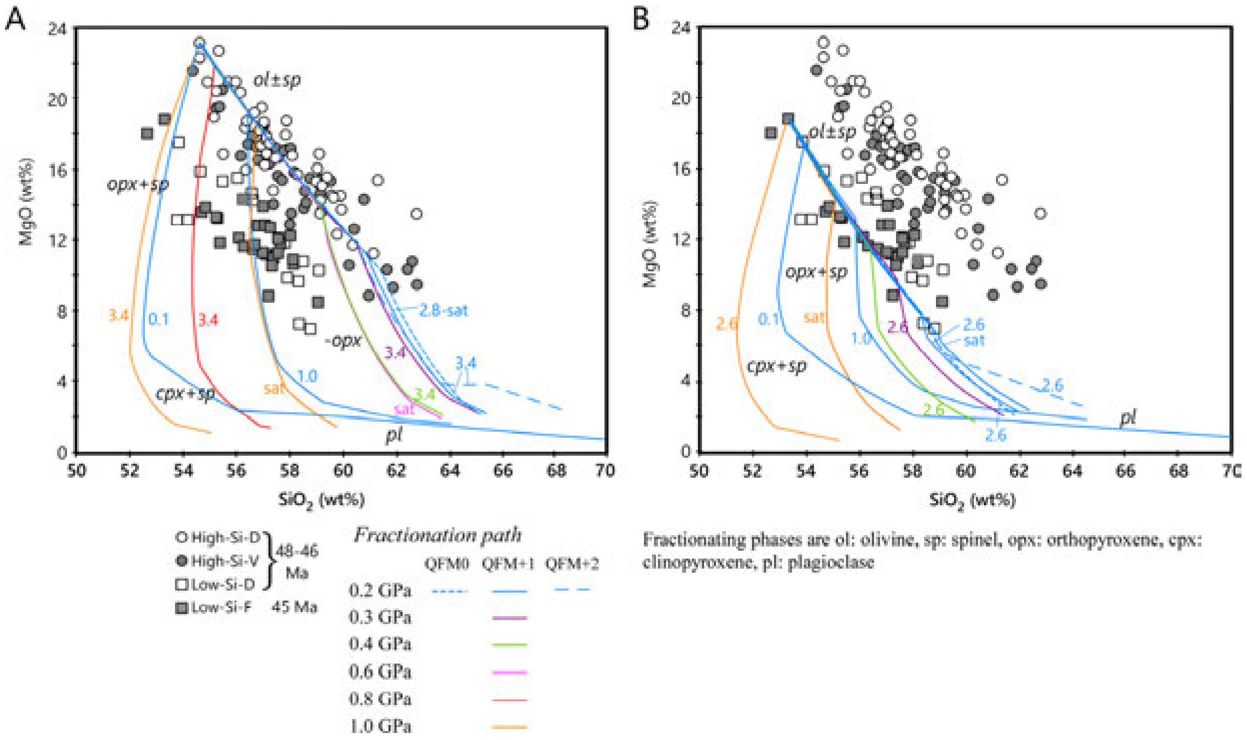

Fractionating phases are ol: olivine, sp: spinel, opx: orthopyroxene, cpx: clinopyroxene, pl: plagioclase

Figure DR-5. Examples of fractional crystallization paths for primary boninite magmas of the high-Si-D (A) and the low-Si-F (B) by alphaMELTS (Smith and Asimow, 2005), compared with boninitic melt inclusions (circles and squares). The numbers beside the paths are H_2O contents (wt%) in the primary magmas. Calculations were done under fO_2 of $\Delta\log(FMQ)=+1$ at pressures 0.2-1.0 GPa, and also under fO_2 of $\Delta\log(FMQ)=0$ and +2 at 0.2 GPa. Change in fO_2 by 2 log units only slightly shifts the fractionation paths. The high-Si boninitic inclusions are mostly plot around low-P (<0.4 GPa), high-H_2O (>2.8 wt%) paths. Higher pressure or lower H_2O content leads to earlier crystallization of orthopyroxene and rapid decreases of MgO, away from the clusters of melt inclusion compositions. The variation of the low-Si inclusions also consistent with low-P (<0.3 GPa), high-H_2O (>2.6 wt%) conditions, suggesting minimal H_2O loss during fractionation. Those plotted at higher MgO than the olivine-fractionation paths suggest mixing of relatively primitive and differentiated melts.

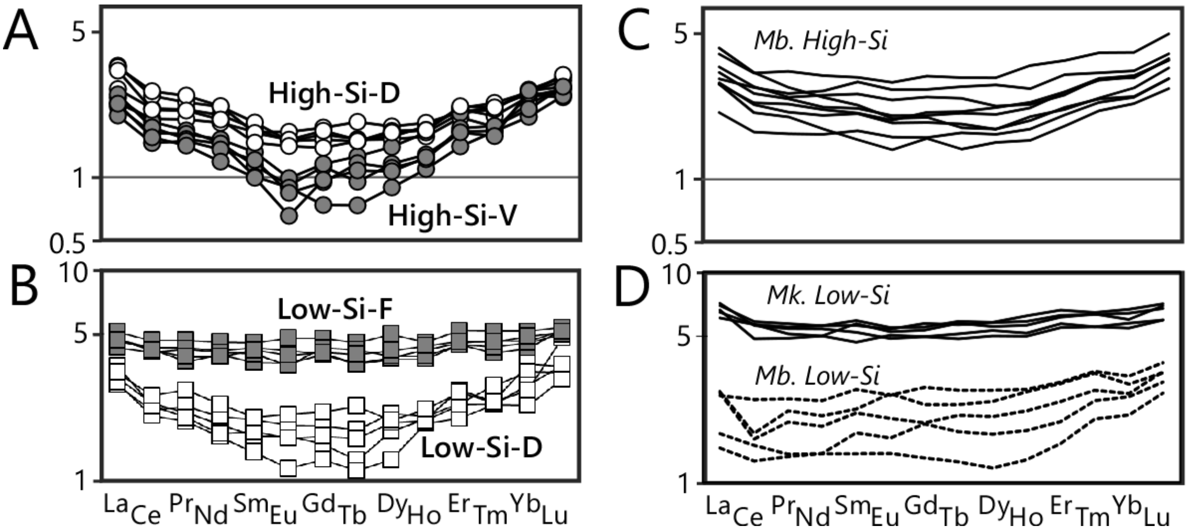

Figure DR-6. Chondrite-normalized REE patterns for the high-Si-D and high-Si-V (A) and the low-Si-D and low-Si-F (B) melt inclusions, compared with the whole-rock compositions (after Kanayama et al., 2012) of high-Si boninite from the 48-46 Ma Maruberiwan Formation (Mb.) (C), and those of low-Si boninites from the 45-Ma Mikazukiyama (Mk.) and 48-46 Ma Maruberiwan (Mb.) Formation (D).

TABLE DR-1. REPRESENTATIVE ANALYSES OF MELT INCLUSIONS IN CHROME SPINEL AND THE ESTIMATED T-P CONDITIONS FOR THE PRIMARY BONINITES

Formation	Maruberiwan												Mikazukiyama			
Geochem.Type	High-Si-V*	High-Si-V	High-Si-V	High-Si-V	High-Si-D*	High-Si-D	High-Si-D	High-Si-D	Low-Si-D*	Low-Si-D	Low-Si-D	Low-Si-D	Low-Si-F*	Low-Si-F	Low-Si-F	Low-Si-F
No. of analyses	3	3	2	3	3	3	3	2	1	2	3	3	5	3	5	2
SiO_2	52.63 ± 0.27	55.89 ± 0.41	58.38 ± 0.51	58.36 ± 0.08	52.20 ± 0.54	56.09 ± 0.42	56.43 ± 0.16	54.95 ± 0.06	53.53 ± 0.22	54.91 ± 0.68	56.12 ± 0.31	57.34 ± 0.17	51.38 ± 0.89	57.75 ± 0.45	53.48 ± 0.31	54.30 ± 0.88
TiO_2	0.09 ± 0.03	0.08 ± 0.05	0.06 ± 0.00	0.07 ± 0.04	0.06 ± 0.02	0.09 ± 0.03	0.08 ± 0.03	0.05 ± 0.04	0.14 ± 0.01	0.10 ± 0.03	0.10 ± 0.04	0.14 ± 0.03	0.12 ± 0.04	0.16 ± 0.04	0.19 ± 0.04	0.13 ± 0.03
Al_2O_3	7.70 ± 0.09	8.16 ± 0.06	10.77 ± 0.14	8.62 ± 0.04	6.42 ± 0.11	7.37 ± 0.15	6.87 ± 0.04	7.10 ± 0.07	10.73 ± 0.10	9.03 ± 0.03	10.05 ± 0.10	11.67 ± 0.07	8.81 ± 0.33	11.58 ± 0.22	10.69 ± 0.33	10.56 ± 0.29
FeO*	8.29 ± 0.16	8.21 ± 0.06	6.49 ± 0.11	7.60 ± 0.20	9.11 ± 0.57	9.19 ± 0.21	8.50 ± 0.17	8.36 ± 0.27	6.37 ± 0.18	10.02 ± 0.04	8.97 ± 0.14	8.20 ± 0.05	8.61 ± 0.26	7.24 ± 0.51	9.41 ± 0.45	6.27 ± 0.32
MnO	0.23 ± 0.05	0.14 ± 0.02	0.19 ± 0.03	0.19 ± 0.05	0.16 ± 0.03	0.23 ± 0.07	0.19 ± 0.03	0.19 ± 0.02	0.10 ± 0.02	0.17 ± 0.05	0.16 ± 0.03	0.13 ± 0.05	0.18 ± 0.08	0.10 ± 0.03	0.24 ± 0.07	0.24 ± 0.08
MgO	20.90 ± 0.63	16.69 ± 0.08	9.76 ± 0.06	15.02 ± 0.11	22.12 ± 0.50	15.1 ± 0.24	18.26 ± 0.11	18.79 ± 0.06	17.41 ± 0.14	15.19 ± 0.10	14.13 ± 0.12	9.49 ± 0.06	18.12 ± 0.66	8.29 ± 0.42	13.52 ± 0.91	10.38 ± 0.68
CaO	5.24 ± 0.12	6.24 ± 0.07	6.93 ± 0.03	6.21 ± 0.10	4.33 ± 0.09	6.25 ± 0.10	5.14 ± 0.03	5.04 ± 0.13	9.02 ± 0.10	6.03 ± 0.04	7.13 ± 0.07	8.34 ± 0.06	7.47 ± 0.31	10.51 ± 0.25	7.97 ± 0.23	9.99 ± 0.35
Na_2O	0.71 ± 0.05	1.25 ± 0.08	1.54 ± 0.00	1.32 ± 0.02	0.33 ± 0.02	1.21 ± 0.03	0.99 ± 0.03	1.27 ± 0.04	0.65 ± 0.04	1.12 ± 0.08	1.38 ± 0.06	1.65 ± 0.04	0.97 ± 0.09	1.48 ± 0.10	1.15 ± 0.09	1.27 ± 0.13
K_2O	0.39 ± 0.06	0.35 ± 0.03	0.26 ± 0.00	0.43 ± 0.01	0.38 ± 0.02	0.31 ± 0.03	0.24 ± 0.05	0.38 ± 0.04	0.16 ± 0.01	0.35 ± 0.04	0.41 ± 0.01	0.39 ± 0.01	0.32 ± 0.05	0.34 ± 0.01	0.32 ± 0.03	0.33 ± 0.05
Cr_2O_3	0.62 ± 0.09	0.19 ± 0.04	0.28 ± 0.05	0.19 ± 0.05	0.45 ± 0.06	0.35 ± 0.06	0.77 ± 0.04	0.31 ± 0.06	1.31 ± 0.05	1.02 ± 0.10	0.65 ± 0.04	0.93 ± 0.02	0.37 ± 0.04	0.31 ± 0.10	0.54 ± 0.07	1.11 ± 0.03
H_2O	2.5 ± 0.5	1.9 ± 0.3	2.8 ± 0.1	3.1 ± 0.1	3.4 ±0.6	3.2 ± 1.6	2.3 ± 0.2	2.1 ± 0.5	2.1±0.1	1.8 ± 0.1	2.2 ± 0.3	1.8 ± 0.3	2.6±0.7	1.2 ± 0.1	2.1 ± 0.3	1.2 ± 0.1
Total	96.81 ± 0.93	97.19 ± 0.34	94.67 ± 0.65	98.01 ± 0.22	95.55 ± 0.96	96.19 ± 0.56	97.47 ± 0.14	96.43 ± 0.21	99.41 ± 0.89	97.94 ± 0.56	99.09 ± 0.33	98.28 ± 0.25	96.37 ± 1.63	97.76 ± 0.41	97.50 ± 1.43	94.56 ± 0.08
$Fe^{3+}/\Sigma Fe$	0.09-0.20				0.09-0.20				0.11-0.24				0.10-0.22			
°C	1423-1428				1415-1419				1343-1347				1378-1384			
GPa	0.89-0.96				0.74-0.80				0.54-0.59				0.81-0.88			
Fo	95.0-95.8				94.4-95.3				95.7-96.4				94.0-95.2			
Tace element compositions [μg/g]																
Li	5.73	7.75		7.27	27.02	5.77	7.20	9.17			6.87	8.81	5.09	5.03	5.09	4.17
B	8.15	10.54		15.82	4.62	10.94	9.08	4.09	10.05		13.52	11.78	6.55	6.57	6.55	8.49
Sc	35.57	33.54		32.98	26.70	31.67	29.81	28.42	51.71		43.12	42.25	56.59	47.19	56.59	45.64
Ti	335.77	409.02		437.78	392.14	534.31	466.18	399.03	624.10		508.74	738.16	1396.72	1214.67	1396.72	866.92
V	159.28	157.75		169.12	134.30	238.77	153.21	141.60	412.26		241.23	244.42	264.64	212.18	264.64	131.51
Co	61.65	54.87		47.33	72.58	59.56	63.84	66.84	96.43		51.21	47.45	49.71	36.89	49.71	31.70
Ni	397.66	259.95		167.02	363.20	108.96	251.07	283.56	233.43		139.76	100.60	132.83	83.60	132.83	84.28
Rb	11.67	11.60		15.21	9.68	9.39	7.01	11.38	7.34		13.35	12.60	5.21	5.05	5.21	5.71
Sr	29.54	39.46		43.52	44.50	60.53	51.22	58.17	53.36		52.24	71.98	93.20	101.86	93.20	103.34
Y	2.04	2.58		2.40	2.86	2.74	3.12	2.90	2.24		2.57	3.36	5.99	7.35	5.99	6.23
Zr	11.72	13.83		16.63	15.15	13.28	14.92	15.93	9.27		13.69	18.76	16.78	17.12	16.78	17.17
Nb	0.31	0.31		0.37	0.38	0.26	0.17	0.52	0.73		0.33	0.42	0.53	0.56	0.53	1.14
Cs	25.66	0.58		0.61	17.52	0.36	0.23	0.54			0.60	0.65	0.18	0.18	0.18	3.96
Ba	27.69	26.83		32.19	13.87	31.11	23.28	40.27	21.08		28.67	33.79	34.98	36.63	34.98	40.23
La	0.47	0.52		0.56	0.69	0.64	0.50	0.97	0.54		0.69	0.78	1.12	1.22	1.12	1.92
Ce	0.90	1.01		1.12	1.39	1.32	1.08	1.83	0.82		1.25	1.57	2.65	2.86	2.65	5.88
Pr	0.14	0.15		0.17	0.23	0.20	0.16	0.27	0.12		0.18	0.25	0.40	0.43	0.40	0.53
Nd	0.62	0.70		0.72	1.13	0.92	0.79	1.19	0.80		0.74	1.06	1.90	2.10	1.90	1.89
Sm	0.18	0.20		0.21	0.31	0.25	0.24	0.33			0.20	0.30	0.64	0.67	0.64	0.47
Eu	0.05	0.06		0.06	0.11	0.08	0.11	0.11	0.09		0.06	0.12	0.23	0.27	0.23	0.19
Gd	0.19	0.23		0.24	0.41	0.32	0.38	0.35	0.35		0.25	0.42	0.80	0.95	0.80	0.78
Tb	0.04	0.05		0.04	0.08	0.06	0.05	0.07			0.04	0.08	0.13	0.16	0.13	0.12
Dy	0.27	0.35		0.31	0.47	0.39	0.44	0.43	0.47		0.31	0.48	0.95	1.23	0.95	1.03
Ho	0.07	0.09		0.08	0.10	0.10	0.08	0.13			0.10	0.12	0.23	0.25	0.23	0.22
Er	0.28	0.33		0.28	0.37	0.34	0.33	0.32	0.36		0.32	0.42	0.73	0.83	0.73	0.70
Tm	0.04	0.05		0.05	0.05	0.05	0.07	0.05			0.06	0.06	0.12	0.13	0.12	0.10
Yb	0.35	0.43		0.36	0.44	0.40	0.40	0.41	0.41		0.37	0.44	0.74	0.83	0.74	0.70
Lu	0.07	0.08		0.07	0.08	0.07	0.07	0.07	0.07		0.07	0.12	0.13	0.13	0.13	0.13
Hf	0.31	0.37		0.45	0.52	0.38	0.40	0.49	0.44		0.47	0.61	0.46	0.50	0.46	0.59
Ta	0.03	0.02		0.02	0.03	0.02		0.03			0.02	0.02	0.03	0.03	0.03	0.07
Pb	1.66	1.39		1.20	1.70	1.50	0.99	1.64	1.02		1.13	1.59	1.07	1.05	1.07	0.87
Th	0.08	0.07		0.06	0.14	0.10	0.06	0.12			0.08	0.10	0.13	0.15	0.13	0.14
U	0.08	0.08		0.07	0.12	0.10	0.07	0.14			0.09	0.08	0.09	0.10	0.09	0.18

Major element oxides are listed in wt%. 1σ of major element oxides are standard deviations of multiple analyses, except the primary Low-Si-D melt inclusion (*) for which 1σ is given as statistic errors of X-ray count.

Primary boninite compositions of the four geochemical types are denoted by asteriscs (*) and are listed with the estimated T-P conditions and Fo contents at olivine and orthopyroxene multiple saturation.

Considering the uncertainties of H_2O contents and f_{O2}, T-P estimates are shown as ranges including 1σ of H_2O and f_{O2} of ΔFMQ 1±1 in log unit.

Table DR-2. Repeated analyses of standard glass NIST610, NIST612, and BIR. Reference values are from Jochum and Nohl (2008).

NIST610	Li	B	Sc	Ti	V	Co	Ni	Rb	Sr	Y	Zr	Nb	Cs	Ba	La	Ce	Pr	Nd	Sm	Eu	Gd	Tb	Dy	Ho	Er	Tm	Yb	Lu	Hf	Ta	Pb	Th	U
Reference value [μg/g]	485	356	441	434	442	405	444	431	497	450	440	419	361	424	457	448	430	431	451	461	420	443	427	449	426	420	462	435	418	377	413	451	457
Average of 24 anal. [μg/g]	491	250	511	502	488	445	405	454	579	584	537	506	405	489	500	519	517	500	525	508	533	549	533	558	558	528	546	551	521	532	463	528	508
Standard deviation [μg/g]	17	61	36	18	12	11	24	9	27	55	42	19.2	10.2	15.0	27.3	16.3	23.3	27.7	31.2	29.9	40.5	50.0	48.3	53.9	51.8	59.0	48.5	62.0	54.9	35.9	12.9	44.2	13.8
RSD (%)	3.4	24.2	7.0	3.6	2.5	2.5	6.0	2.0	4.7	9.4	7.9	3.8	2.5	3.1	5.5	3.1	4.5	5.5	5.9	5.9	7.6	9.1	9.1	9.7	9.3	11.2	8.9	11.3	10.5	6.7	2.8	8.4	2.7
Accuracy (%)	1.4	-42.5	13.7	13.6	9.4	9.0	-9.7	5.1	14.1	23.0	18.0	17.1	10.8	13.3	8.6	13.8	16.8	13.8	14.1	9.2	21.3	19.3	19.9	19.4	23.7	20.4	15.4	21.1	19.9	29.2	10.8	14.7	10.0

NIST612	Li	B	Sc	Ti	V	Co	Ni	Rb	Sr	Y	Zr	Nb	Cs	Ba	La	Ce	Pr	Nd	Sm	Eu	Gd	Tb	Dy	Ho	Er	Tm	Yb	Lu	Hf	Ta	Pb	Th	U
Reference value [μg/g]	42	43	44	45	46	47	48	49	50	51	52	53	54	55	56	57	58	59	60	61	62	63	64	65	66	67	68	69	70	71	72	73	74
Average of 9 anal. [μg/g]	42	26	41	43	41	40	36	33	84	44	42	40	46	41	38	43	41	39	41	38	41	43	41	42	44	42	43	42	41	42	43	41	41
Standard deviation [μg/g]	1	2	0	1	0	0	1	0	1	1	1	0.6	0.7	0.3	0.6	0.3	0.4	0.3	0.3	0.4	0.7	0.5	0.7	1.1	1.2	0.6	0.6	0.7	0.1	0.0	0.4	0.3	0.4
RSD (%)	2.5	6.2	1.1	2.2	0.9	0.8	3.5	1.5	0.9	2.0	2.3	1.5	1.6	0.6	1.6	0.8	1.0	0.9	0.7	1.1	1.7	1.2	1.8	2.6	2.7	1.5	1.4	1.6	0.2	0.0	0.9	0.7	1.1
Accuracy (%)	1.0	-63.2	-5.8	-3.5	-10.2	-16.5	-31.9	-46.0	41.0	-14.3	-21.8	-31.9	-16.8	-32.2	-45.3	-32.4	-39.3	-50.2	-46.4	-60.6	-51.4	-45.6	-55.6	-51.9	-50.5	-58.8	-57.7	-62.2	-70.3	-66.7	-66.4	-77.6	-79.4

BIR-1G	Li	B	Sc	Ti	V	Co	Ni	Rb	Sr	Y	Zr	Nb	Cs	Ba	La	Ce	Pr	Nd	Sm	Eu	Gd	Tb	Dy	Ho	Er	Tm	Yb	Lu	Hf	Ta	Pb	Th	U
Reference value [μg/g]	3		43	5400	326	52	178	0.2	109	14	14	0.52	0.01	6.50	0.61	1.89	0.37	2.37	1.09	0.52	1.85	0.35	2.55	0.56	1.70	0.24	1.64	0.25	0.57	0.04	3.70	0.03	0.02
Average of 13 anal. [μg/g]	3	2	41	5740	327	54	143	0	110	14	14	1	0	7	1	2	0	2	1	1	2	0	2	1	2	0	2	0	1	0	4	0	0
Standard deviation [μg/g]	0	1	1	114	8	1	12	0	3	0	0	0	0	0	0	0	0	0	0	0	0	0	0	0	0	0	0	0	0	0	0	0	0
RSD (%)	3.1	53.0	2.3	2.0	2.3	2.0	8.5	5.5	2.4	3.0	2.5	6.2	71.4	3.7	4.5	3.1	4.2	4.4	3.4	3.8	4.2	6.8	5.0	6.2	3.5	5.6	5.0	9.0	8.4	27.9	3.7	16.9	30.8
Accuracy (%)	-0.7		-4.4	5.9	0.4	4.5	-24.3	-0.3	0.8	0.2	-2.9	-1.9	-36.8	1.4	-3.3	3.8	0.3	-1.0	-0.2	0.1	-9.0	-2.9	-2.9	-5.7	-4.8	-3.2	-2.3	-7.3	-3.8	3.2	-3.4	-6.2	-37.2